

Peculiarities of the phase transformation dynamics in bulk FeRh based alloys from magnetic and structural measurements

Vladimir I. Zverev

Radel R. Gimaev

Faculty of Physics, M.V. Lomonosov Moscow State University, 119991 Moscow, Russia

Takafumi Miyanaga

Department of Mathematics and Physics, Hirosaki University, Hirosaki, Aomori 036-8561, Japan

Artem A. Vaulin

M.N. Mikheev Institute of Metal Physics, Ural Branch, Russian Academy of Sciences, 620108, Yekaterinburg, Russia

Andrey F. Gubkin

M.N. Mikheev Institute of Metal Physics, Ural Branch, Russian Academy of Sciences, 620108, Yekaterinburg, Russia

Institute of Natural Sciences and Mathematics, Ural Federal University, Yekaterinburg, 620083, Russia

Boris B. Kovalev

National Research Center "Kurchatov Institute", Moscow 123182, Russia

Antonio M. dos Santos

Neutron Scattering Division, Oak Ridge National Laboratory, Oak Ridge, TN 37831-6475, USA

Edmund Lovell

Lesley F. Cohen

Blackett Laboratory, Imperial College, Prince Consort Road, London SW7 2AZ, UK

Nikolai A. Zarkevich

Ames Laboratory, U.S. Department of Energy, Ames, Iowa 50011, USA

ABSTRACT

We analyze coexistence of antiferromagnetic and ferromagnetic phases in bulk iron-rhodium and its alloys with palladium, $\text{Fe}_{50,4}\text{Rh}_{49,6}$, $\text{Fe}_{49,7}\text{Rh}_{47,4}\text{Pd}_{2,9}$ and $\text{Fe}_{48,3}\text{Rh}_{46,8}\text{Pd}_{4,9}$, using neutron diffraction, magnetization and scanning Hall probe imaging. Temperature dependencies of the lattice parameters, AFM and FM phase weight fractions, and Fe magnetic moment values were

obtained on cooling and heating across the AFM-FM transition. Substantial thermomagnetic hysteresis for the phases' weight fractions and a relatively narrow one for the unit cell volume has been observed on cooling-heating. A clear dependence of hysteretic behavior on Pd concentration has been traced. Additional direct magnetic measurements of the spatial distribution of the phase transition are acquired using scanning Hall probe microscopy, which reveals the length scale of the phase coexistence and the spatial progression of the transition in the presence of external magnetic field. Also, the magnetic phase diagram has been constructed for a series of Pd-doped FeRh alloys.

INTRODUCTION

Phase coexistence is a rather general and curious phenomenon for many materials experiencing first-order magnetic phase transitions (FOMT) [1–3]. At the same time, explanations of this phenomenon within the mechanisms of interaction of electrons or imperfections of chemical composition and structure still seem inconclusive [4,5]. An example of a material that undergoes antiferromagnetic-ferromagnetic (AFM-FM) FOMT with temperature co-existence of phases is an iron-rhodium alloy and its derivatives. In recent years, interest from the scientific community in e-Rh alloys has increased significantly [6–12]. The attention to these alloys is due to two main reasons: firstly, the fundamental research of these alloys aims to find out the origin of FOMT and explain the cause of a giant magnetocaloric effect (MCE) which results, and secondly, the B2 alloys are promising for practical applications (an example is Ni-Co-Mn-Ti [13]). The observation of the FOMT at temperatures close to the temperature of the human body in these alloys, in combination with a giant MCE [14], make Fe-Rh-based materials promising for use in areas less sensitive to the cost of the alloy, primarily in medicine (for example, in the technology of targeted drug delivery [15,16]), magnetic recording [17], etc. In the majority of works studying the origin of the magnetic phase transition in iron-rhodium alloys, attention focused on various energy contributions to the free energy: phonon, conduction electron and magnons [18], exchange energy associated with magneto-volume effects [19], and lattice dynamics [20], which can be clarified by direct observation of the phase transformation [21]. At the same time, the influence of phase coexistence on the functional properties of the material is much less studied, except for a few works on thin films: see examples of Fe₄₉Rh₅₁ [22] and FeRh_{0.82}Pd_{0.18} [23]. A heterogeneous nucleation of ferromagnetic domains on micron and submicron scales in close proximity to the AFM-FM phase transition temperature was reported in those studies.

It is important to note that there are not many works devoted to the study of FeRh-based alloys doped with a third metal, as well as a lack of data obtained by direct methods, such as neutron scattering or magnetic imaging. Particularly, no such measurements have ever been

performed on the doped alloys. In Ref. [24], Pd-doped samples $\text{Fe}_{48}\text{Rh}_{46}\text{Pd}_6$ and $\text{Fe}_{48}\text{Rh}_{49}\text{Pd}_3$ were considered for the first time. Both of them exhibit a decrease of phase transition temperature: 169 K for $\text{Fe}_{48}\text{Rh}_{46}\text{Pd}_6$ and 252 K for $\text{Fe}_{48}\text{Rh}_{49}\text{Pd}_3$ in comparison with the pure iron-rhodium alloy (328 K). The next systematic study of these alloys was performed almost 30 years later [25]. In this work, magnetization, electrical resistance, magnetoresistance and heat capacity were measured in alloys with low palladium content: $\text{Fe}_{49}(\text{Rh}_{1-x}\text{Pd}_x)_{51}$, $x=0\div 0.14$. It has been found that the magnetic state and electrical properties of the described compounds strongly depend on the number of replacement atoms due to the electronic origin of magnetic phase transitions. The phase transition in all studied alloys is accompanied by a giant magnetoresistance ($\Delta\rho/\rho$ up to -88%). Magnetic phase diagrams were also constructed for the studied alloys.

The renewed interest to iron-rhodium alloys was due to the study of the impact of the manufacturing process on the physical and chemical properties of pure FeRh samples, such as $\text{Fe}_{49.5}\text{Rh}_{50.5}$ and $\text{Fe}_{52}\text{Rh}_{48}$ [26].

For the first time the transition dynamics and phase co-existence in a bulk sample doped with palladium $\text{Fe}_{49}(\text{Rh}_{0.93}\text{Pd}_{0.07})_{51}$ was described in [27,28], where indirect methods, such as electrical and magnetoresistance measurements, were used. The authors focused on the study of the transition dynamics in high magnetic fields. A composition with a minimum temperature of the AFM-FM transition in a series of alloys with a varying Pd at.% was chosen. The relaxation time of the magnetic subsystem increased significantly in magnetic fields above 6 T at temperatures below 50 K. An increase of the external magnetic field up to 8 T completely suppressed the AFM-FM transition, while coexistence of the FM and AFM short-range magnetic orders persisted down to low temperatures and gave rise to the glass-like arrested state (GLAS). The GLAS state was removed by heating sample to the temperatures above 50 K [28].

Neutron studies of the iron-rhodium alloys, and especially Pd-doped alloys, are also very rare. The first work of this type was performed on $\text{Fe}_{44}\text{Rh}_{56}$ sample [29]. The space group $Fm\bar{3}m$, the unit cell parameter $a=2.98 \text{ \AA}$, as well as a qualitative estimate of magnetic moments of Fe and Rh atoms were obtained from the neutron diffraction data. Magnetic moments of Fe and Rh atoms $\mu_{\text{Fe}}=3.2 \mu_{\text{B}}$, $\mu_{\text{Rh}}=0.9 \mu_{\text{B}}$ were determined by neutron diffraction and Mossbauer spectroscopy in $\text{Fe}_{50}\text{Rh}_{50}$, $\text{Fe}_{65}\text{Rh}_{35}$, $\text{Fe}_{60}\text{Rh}_{40}$ and $\text{Fe}_{52}\text{Rh}_{48}$ [30,31]. Moreover, the form-factors of magnetic neutron scattering for Fe and Rh atoms obtained in these works were used for the Rietveld analysis of the neutron diffraction data in this work (see experimental details). Shortly after these studies, coexistence of the AFM and FM phases across the transition was studied by a neutron diffraction method [32]. In pure FeRh samples (without any substitutional elements) of nearly equiatomic composition, the region with coexistence of AFM and FM phases was found. The conclusion about the coexistence of AFM and FM phases in a certain temperature range was based only on a

qualitative analysis. In contrast to the previous work [32], here we first conduct a thorough quantitative Rietveld analysis for pure iron-rhodium alloy and for palladium-doped companion samples. The texture effect is also noted, despite the fact that the sample for neutron studies is a powder. We define the quantitative temperature dependence of the AFM and FM phase fractions. In addition, we present quantitative temperature dependences of lattice parameters and the value of the magnetic moment of iron atoms in both phases for all three samples.

The most recent theoretical work to date, which addresses the issue of phase co-existence, is [20]. The lattice dynamics of the antiferromagnetic and ferromagnetic phases of FeRh at different temperatures were investigated from first principles. It has been shown that already at low temperature the bcc structure of the antiferromagnetic phase becomes stable; this eliminates the contradiction between experimental observations and previous theoretical prediction of a lattice instability at low temperature [33]. In addition, a significant difference in the temperature dependence of lattice vibrations of the ferromagnetic and antiferromagnetic phases has been observed. It was concluded that the lattice dynamics plays a decisive role in the metamagnetic phase transition in FeRh and its remarkable magnetocaloric properties. Table 1 in [20] presents the latest up-to-date calculated values of the lattice parameters in AFM and FM phases, respectively, 2.990 and 3.007 Å, and also magnetic moment values of Fe ($3.12 \mu_B$ and $3.17 \mu_B$) and Rh atoms ($0.00 \mu_B$ and $1.05 \mu_B$, respectively) in the stoichiometric FeRh.

In our work we analyze various non-stoichiometric compositions of iron-rhodium alloys: Fe_{50,4}Rh_{49,6}, Fe_{49,7}Rh_{47,4}Pd_{2,9} and Fe_{48,3}Rh_{46,8}Pd_{4,9}. The Fe_{50,4}Rh_{49,6} without Pd is considered to be a reference sample. The results obtained on the palladium-doped samples Fe_{49,7}Rh_{47,4}Pd_{2,9} and Fe_{48,3}Rh_{46,8}Pd_{4,9} are compared with the reference one and with each other for the first time. Thus, one can have a full understanding of the phase transformation evolution and its dependence on the Pd concentration in the series of alloys.

As has been shown above, quite often in the previous studies of FeRh-based alloys, very targeted characterization tools have been used. Therefore, this has sometimes led to a lack of necessary experimental data on the samples, such as precise composition and phase fraction: crucial in the case of FeRh. Here we complete thorough studies on our samples, for which the results of structural, magnetic, and magnetocaloric experiments have been published [34,35].

THEORETICAL CONSIDERATION

To address disorder on each sublattice, we used the scripts [36] and the KKR-CPA method [37] implemented in MECCA code [38]. We used the PBEsol exchange correlation [39] and 16^3 Monkhorst-Pack k -mesh [40] for the Brillouin zone integration. Computational details and the computed electronic density of states (DOS) in the equiatomic binary FeRh are provided in [41].

Rh has 1 extra d -electron compared to Fe, and Pd has 1 more electron than Rh. In the rigid-band approximation, the difference in the electron count between $\text{Fe}_{0.5-y}\text{Rh}_{0.5+y-x}\text{Pd}_x$ and an equiatomic FeRh constitutes $(y+x)$ d -electrons per atom, or $2(y+x)$ per B2 2-atom unit cell. Relative to FeRh, the shifts of the electron count in $\text{Fe}_{49.7}\text{Rh}_{47.4}\text{Pd}_{2.9}$ and $\text{Fe}_{48.3}\text{Rh}_{46.8}\text{Pd}_{4.9}$ are $(0.003+0.029)=0.032$ and $(0.017+0.049)=0.066$ e/atom , respectively, while the expected shifts of the Fermi energy are $+0.022$ and $+0.045$ eV in the FM state, and $+0.011$ and $+0.022$ eV in the AFM state. Fig. 1(a) shows the computed electronic spin DOS in the FM state in $\text{Fe}_{49.7}\text{Rh}_{47.4}\text{Pd}_{2.9}$ and $\text{Fe}_{48.3}\text{Rh}_{46.8}\text{Pd}_{4.9}$. The B2 structure has two sublattices; we have assumed that sublattice 1 is occupied by Fe_1 and Rh_1 , while sublattice 2 is populated by Rh_2 and Pd_2 , so that Pd partially substitutes Rh_2 , with sublattice compositions $(\text{Fe}_{0.994}\text{Rh}_{0.006})(\text{Rh}_{0.942}\text{Pd}_{0.058})$ and $(\text{Fe}_{0.966}\text{Rh}_{0.034})(\text{Rh}_{0.902}\text{Pd}_{0.098})$ in $\text{Fe}_{49.7}\text{Rh}_{47.4}\text{Pd}_{2.9}$ and $\text{Fe}_{48.3}\text{Rh}_{46.8}\text{Pd}_{4.9}$, respectively. The coherent potential approximation (CPA) assumes a homogeneous disorder on each sublattice, without any short-range ordering (SRO). A change of the long-range order (LRO) from ordered B2 to disordered A2 results in the increase of energy at fixed composition: see Fig. 2(c). According to our calculations, the transition temperature for a hypothetical order-disorder B2 to A2 transition is expected to be well above the Curie temperature, therefore the energetically unfavorable A2 structure will not be observed. Here we consider the energetically favorable B2 ordering, relevant to experiment.

The computed bulk modulus B_0 in these alloys is around 200 GPa (2×10^{11} Pa), and B_0' is around 4 (dimensionless). In the FM state, the computed equilibrium lattice constant of $\text{Fe}_{48.3}\text{Rh}_{46.8}\text{Pd}_{4.9}$ is 2.995 Å, 0.003 Å larger than that of $\text{Fe}_{49.7}\text{Rh}_{47.4}\text{Pd}_{2.9}$. Fig.1 shows that Pd has a higher contribution to the electronic DOS at the Fermi energy E_F than Rh on the Rh sublattice 2. Electronic entropy increases with electronic DOS at E_F , affecting the caloric response.

In the FM state, Pd atomic magnetic moment is smaller than that of Rh: see Table 1. On the Rh sublattice, the Rh moment changes from ~ 1 Bohr magneton (μ_B) in the FM to 0 in the AFM state. FeRh is an itinerant ferromagnet, in which the total magnetization is well-defined, while the computed atomic moments depend on the chosen sizes of atomic spheres or polyhedra [42]. Magnetic entropy in the PM state scales with the atomic magnetic moments. However, the magnetic entropy is small in states with magnetic long-range order (LRO), such as FM and AFM.

The phase transition temperature depends on the energy difference between the relevant phases. The lattice mismatch at the phase transition affects the thermal hysteresis; it is smaller in $\text{Fe}_{48.3}\text{Rh}_{46.8}\text{Pd}_{4.9}$ compared to $\text{Fe}_{50.4}\text{Rh}_{49.6}$, as shown in Fig.2. We used the coherent potential approximation (CPA), which approximates an atomic disorder by a homogeneously random uncorrelated disorder without short-range order (SRO), and magnetic disorder in the PM state by

homogeneously disordered local moments (DLM). Because SRO lowers the energy, CPA systematically overestimates the energy of the PM state. In general, properties depend on composition, atomic and magnetic ordering. Assuming that Pd equally substitutes Rh (on both Fe and Rh sublattices), we computed energy versus the lattice constant in B2 phase in $\text{Fe}_{48.3}\text{Rh}_{46.8}\text{Pd}_{4.9}$ and $\text{Fe}_{50.4}\text{Rh}_{49.6}$: see Fig. 2. In this approximation, the computed equilibrium lattice constants in AFM, FM, and PM states are respectively 2.974, 2.989, and 2.978 Å in $\text{Fe}_{50.4}\text{Rh}_{49.6}$; they increase to 2.982, 2.996, and 2.986 Å in $\text{Fe}_{48.3}\text{Rh}_{46.8}\text{Pd}_{4.9}$. Depending on the atomic order, there is a small difference between the computed FM value of 2.996 Å in $(\text{Fe}_{0.966}\text{Rh}_{0.030}\text{Pd}_{0.004})(\text{Rh}_{0.895}\text{Pd}_{0.105})$ and 2.995 Å in $(\text{Fe}_{0.966}\text{Rh}_{0.034})(\text{Rh}_{0.902}\text{Pd}_{0.098})$, both representing B2 $\text{Fe}_{48.3}\text{Rh}_{46.8}\text{Pd}_{4.9}$. Atomic order (both LRO and SRO) depends on the heat treatment. The LRO can vary from highly ordered B2 to disordered A2; there is a partial LRO in the quenched samples. Sensitivity of transition temperature to ordering and composition is discussed in [41].

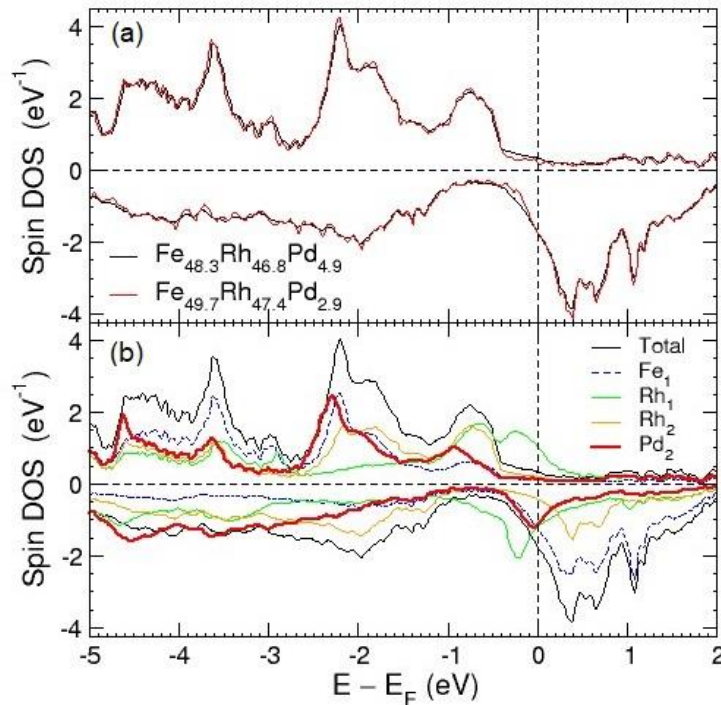


Fig. 1. The computed electronic spin DOS in the FM state in $\text{Fe}_{49.7}\text{Rh}_{47.4}\text{Pd}_{2.9}$ and $\text{Fe}_{48.3}\text{Rh}_{46.8}\text{Pd}_{4.9}$ (a) and atom-projected spin DOS in $\text{Fe}_{48.3}\text{Rh}_{46.8}\text{Pd}_{4.9}$ (b).

Table 1. Computed atomic magnetic moments (μ_B per atom) and the total magnetization M (μ_B per B2 unit cell) at fixed $a=3.0$ Å in the FM state.

	$\text{Fe}_{48.3}\text{Rh}_{46.8}\text{Pd}_{4.9}$	$\text{Fe}_{49.7}\text{Rh}_{47.4}\text{Pd}_{2.9}$	$\text{Fe}_{50}\text{Rh}_{50}$
Fe ₁	3.31	3.31	3.318
Rh ₁	0.55	0.59	-
Rh ₂	0.97	0.99	0.998

Pd ₂	0.35	0.35	-
<i>M</i>	4.13	4.25	4.2

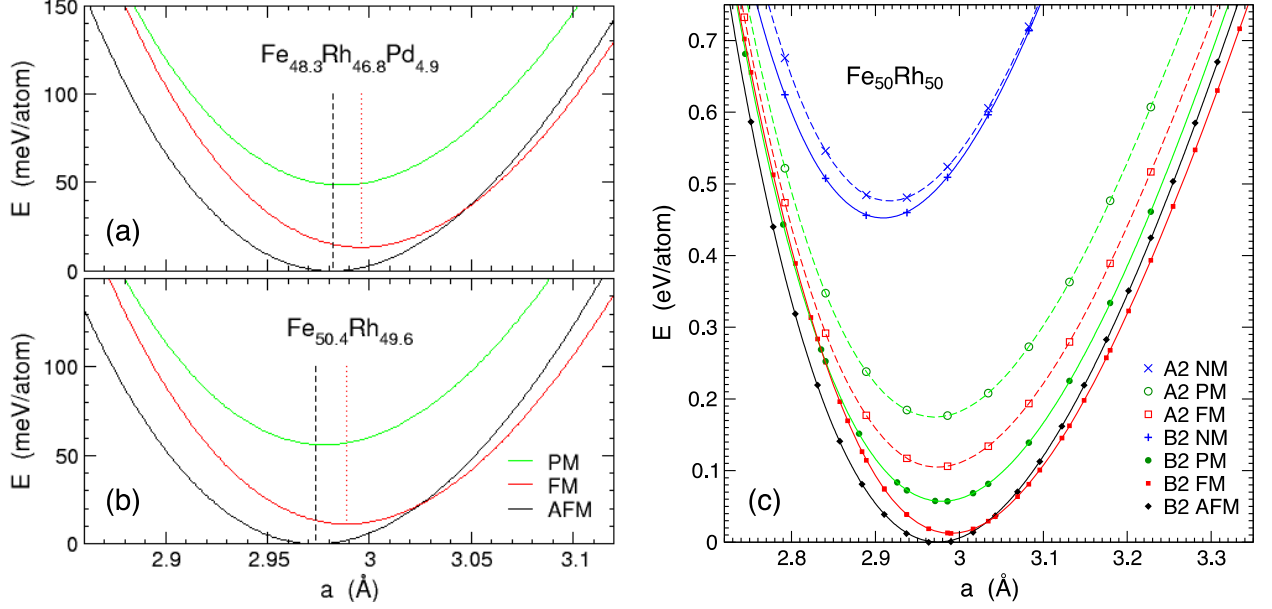


Fig. 2. Energy E versus lattice constant a , fitted by the Birch–Murnaghan equation of state in AFM, FM, and PM states in B2 Fe_{48.3}Rh_{46.8}Pd_{4.9} (a) and B2 Fe_{50.4}Rh_{49.6} (b), compared to DFT (symbols) approximated by cubic splines (lines) in A2 (dashed lines, empty symbols) and B2 (solid lines, filled symbols) equiatomic FeRh (c). The vertical black dashed (red dotted) lines point at the equilibrium lattice constant in the AFM (FM) state, respectively.

SAMPLES AND EXPERIMENTAL TECHNIQUE

Polycrystalline bulk samples Fe_{50.4}Rh_{49.6}, Fe_{49.7}Rh_{47.4}Pd_{2.9} and Fe_{48.3}Rh_{46.8}Pd_{4.9} were manufactured in the Department of Advanced Physics, Hirosaki University, Japan from high-purity Fe, Rh, Pd. Source materials had a purity of 99.9 at.%. The chemical composition of the used samples was determined by the X-ray microanalysis (EPMA) method. Bulk samples of iron-rhodium alloys were made of ingots from plasma arc melting.

Stoichiometric amounts of the starting metals are placed in an airtight melting chamber, from which the air is pumped out to a pressure of 10^{-3} Pa. After pumping, the chamber is filled with argon to the pressure of 0.09 MPa. Source metals in the plasma arc furnace are melted due to the plasma arc that occurs between the plasmatron cathode and the molten metal. The temperature of the plasma arc reaches values of up to 15 000 K. The argon gas in the chamber served as the plasma gas.

The resulting alloy ingots were in the form of ellipsoids of rotation with axes in the range of 3 - 5 mm. Samples were cut from ingots, which were annealed in a vacuum at 1273 K for 24 hours. During annealing, the fcc crystalline structure formed in the alloy after melting changes to bcc with ordered magnetic structure and homogenization of the alloy. Then the samples were hardened, with their rapid cooling to room temperature. For this purpose, after annealing in the furnace, the samples at 1273 K were put in cold water. There is about 7% of γ -FeRh (FCC) phase in each sample within the whole temperature range. Therefore, FM and AFM phase occupy ~93% in total volume.

Neutron diffraction

Time of flight neutron scattering experiments were performed at the NOMAD beamline [43] at the Spallation Neutron Source, ORNL, USA. This beamline is dedicated to extended momentum transfer measurements and the combination of short flight path (19.5 m) combined with one of the highest neutron flux available, allows measurements on very small samples. The beam frequency was set at 60 Hz and the wavelength band was nominally centered at 1.5 Å, allowing for an available wavelength range of 0.3 Å - 3 Å. NOMAD is equipped with four detector banks located at the scattering angles $2\theta=31^\circ$, 67° , 122° , 154° . We used neutron diffraction patterns obtained from two detector banks located at $2\theta=31^\circ$ (D1 bank) and $2\theta=122^\circ$ (D3 bank). D1 bank covers magnetic Bragg peaks in the low q -range while the D3 bank provides the best resolution covering the high q -range. Three samples were measured with compositions $\text{Fe}_{50,4}\text{Rh}_{49,6}$, $\text{Fe}_{49,7}\text{Rh}_{47,4}\text{Pd}_{2,9}$ and $\text{Fe}_{48,3}\text{Rh}_{46,8}\text{Pd}_{4,9}$. Prior to the neutron diffraction measurements, a small amount of each sample, about 300 mg, was ground in a He filled glove box and sealed in thin walled vanadium cans with 6 mm diameter. Temperature was controlled in the experiment via an Ar gas flow cryostream. All the neutron diffraction patterns were measured first on cooling from 320 K down to 218 K, then on heating from 218 K up to 320 K. The temperature setpoint was nominally set to $\Delta T = 3$ K intervals, with a 30 s delay for temperature stabilization. The sample temperature was logged at a sensor placed in the output nozzle of the cryostream, as is customary in such setup, therefore some lag between the recorded temperature and the real sample temperature is to be expected. The resulting cooling/heating rate was ~0.6 K/min and the data acquisition time for 1 neutron diffraction pattern was 4 minutes.

The Rietveld refinement of the neutron diffraction data obtained from D1 and D3 banks was performed in a multipattern mode using Fullprof Suite package [44]. Magnetic form factors for both Fe and Rh atoms in the Fe-Rh compounds were obtained experimentally by polarized neutron technique [31]. In order to compare experimentally determined form factors for metallic

FeRh compound with the ones tabulated in Fullprof for different Fe and Rh ions, we plotted them in Fig. 3 Form factors for Fe^{3+} , Fe^{2+} , Fe^{1+} and Rh^{1+} ions tabulated in Fullprof are shown (symbols), with experimentally determined form factors for Fe and Rh atoms in the metallic FeRh systems (lines) from [31]. As one can see, magnetic scattering form factor of Fe^{3+} ion tabulated in Fullprof is in good agreement with the experimentally observed form factors for Fe atom in metallic $\text{Fe}_{50}\text{Rh}_{50}$ compound. Experimentally obtained Rh form factor fits well to the Rh^{1+} ion form factor tabulated in Fullprof. Therefore, we used standard Fe^{3+} and Rh^{1+} form factors tabulated in Fullprof to perform the Rietveld refinement of the neutron diffraction patterns for all the studied samples.

The similar problem has been studied by neutron diffraction and estimations of the lower limit of the FM and AFM domain sizes were obtained for $(\text{La}_{1-y}\text{Pr}_y)_{0.7}\text{Ca}_{0.3}\text{MnO}_3$ [45].

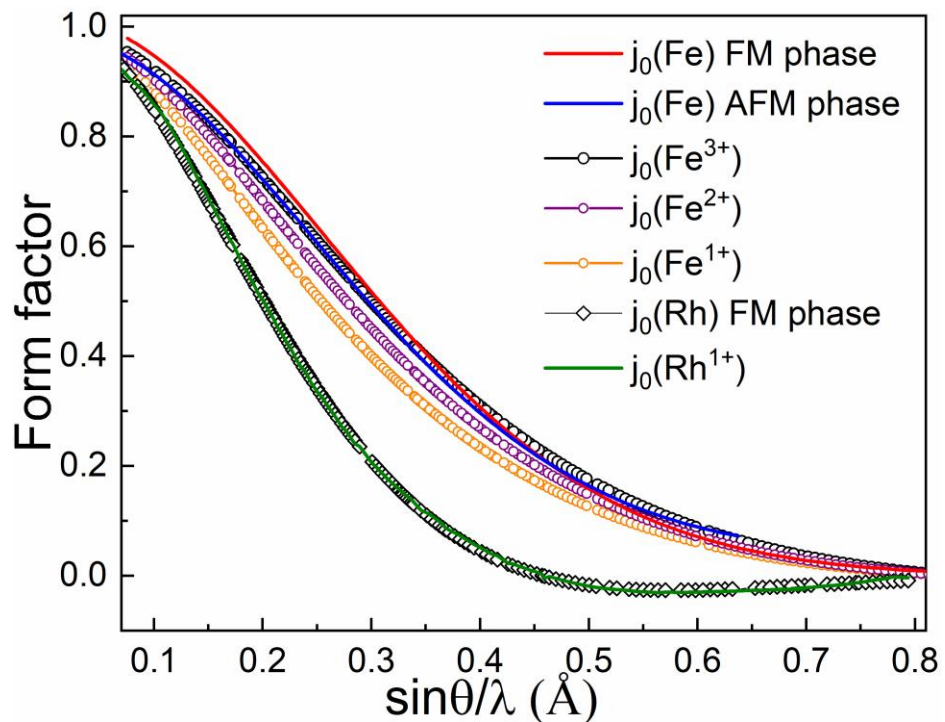


Fig. 3 Form factors for Fe^{3+} , Fe^{2+} , Fe^{1+} and Rh^{1+} ions tabulated in Fullprof are shown (symbols), with experimentally determined form factors for Fe and Rh atoms in the metallic FeRh systems (lines) from [31].

Hall probe imaging

Spatial magnetic information of the thermal transition in 1 T magnetic field was obtained on an approximately $3 \times 3 \times 2 \text{ mm}^2$ cuboid sample of $\text{Fe}_{48,3}\text{Rh}_{46,8}\text{Pd}_{4,9}$ (the surface imaged is marked in the upper inset of Fig. 8 Moment (normalised to the saturated FM moment) of the thermal transition, extracted from Hall probe imaging data in 1 T. Inset: **upper**: the imaged surface of the cuboid $\text{Fe}_{48,3}\text{Rh}_{46,8}\text{Pd}_{4,9}$ sample with the field direction shown by an arrow; **bottom**: the image at 286.5 K on warming (designated by the red circle), part-way through the transition, subtracting the image at 260 K before the transition (black circle), showing the change in the spatial

distribution of moment.) using scanning Hall probe microscopy with a $5 \times 5 \mu\text{m}^2$ active-area Hall sensor fabricated in a $2.5 \mu\text{m}$ thick Te-doped InSb epilayer on an undoped GaAs substrate. The sensor active area size principally determines the smallest possible spatial resolution of magnetic information and is smaller than the pixel size of the images of $15 \times 15 \mu\text{m}^2$. The sensor was scanned over one of the sample's $3 \times 3 \text{mm}^2$ faces, in contact with a film of Teflon positioned on the surface, which permitted smooth sensor motion at a constant height of $10 \mu\text{m}$ above the sample. The applied field direction was perpendicular to this surface, in the direction of probe sensitivity. The scanning Hall probe microscopy was performed in a 4 T split-coil superconducting magnet and continuous flow helium Oxford Instruments Cryostat. Prior to imaging, the sample was heated to 350 K in zero field, then cooled to 290 K, at which temperature 1 T magnetic field was applied. Images were taken at a series of constant T values between cooling steps to 194 K and subsequent heating steps to 291 K; prior to the acquisition of each image, T was stabilized for 10 min, and the duration of each acquisition itself was approximately 30 min. During image processing, the applied field is subtracted from each image, leaving only magnetic field information produced by the sample moment.

RESULTS AND DISCUSSION

Neutron diffraction

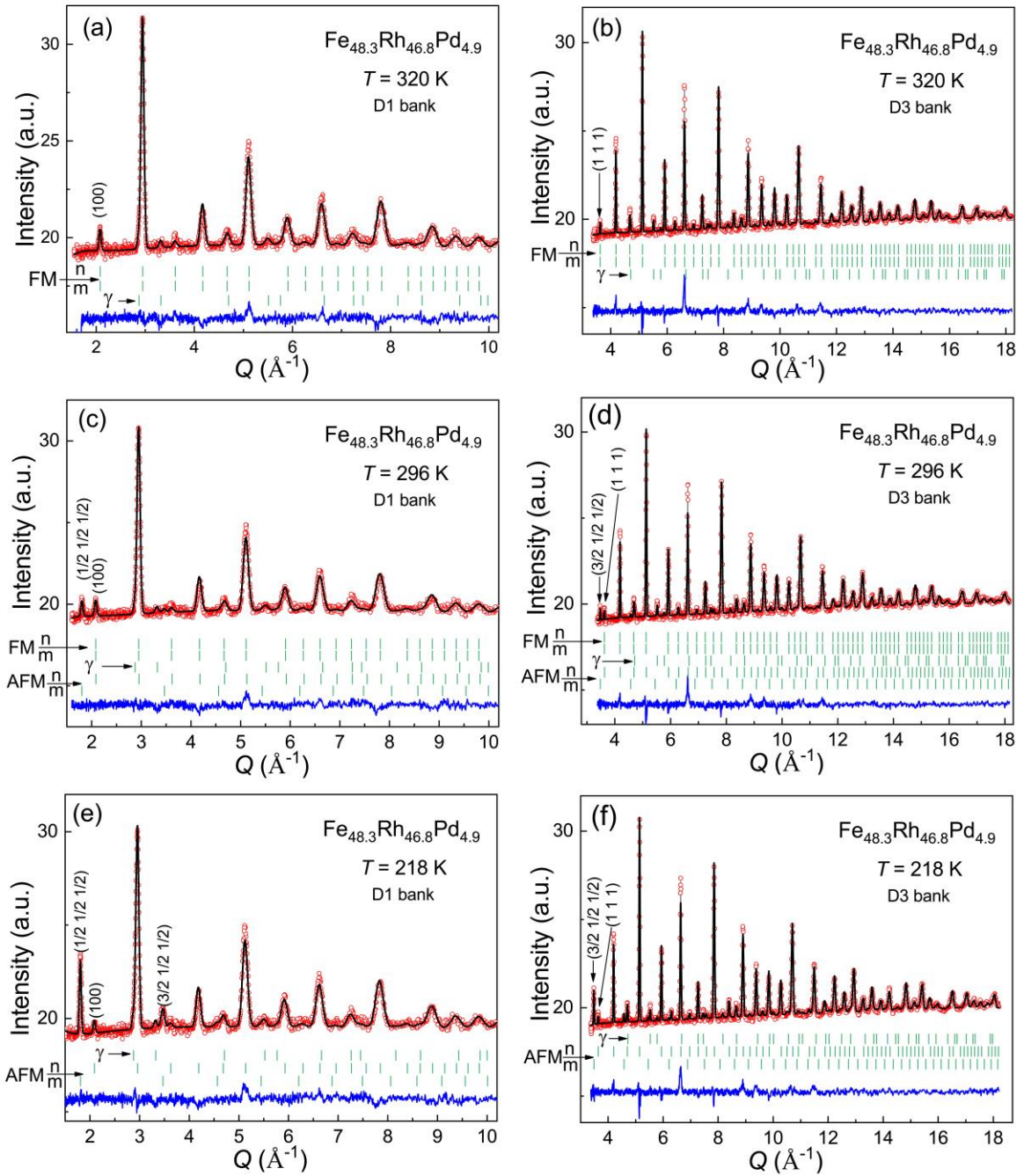


Fig. 4 The best fit result of the neutron diffraction patterns measured (a,b) in the FM state at 320 K, (c,d) in the mixed magnetic state at the AFM-FM phase transition temperature, and (e,f) in the AFM magnetic state at 218 K for the $\text{Fe}_{48.3}\text{Rh}_{46.8}\text{Pd}_{4.9}$ sample. Data is plotted as a function of momentum transfer, defined as $Q=2\pi/d$, where d is the interplanar spacing. The red symbols are experimental points and the solid black line represents the result of the fit. The difference between calculated and observed intensities is shown at the bottom. The rows of vertical marks below the patterns refers to the Bragg peaks positions. FM and AFM denote rows of Bragg peaks positions given for ferromagnetic and antiferromagnetic phases, respectively, n is for nuclear and m is for magnetic contribution, γ denotes the Bragg peaks coming from the fcc γ -phase.

Neutron diffraction patterns obtained for $\text{Fe}_{48.3}\text{Rh}_{46.8}\text{Pd}_{4.9}$ and $\text{Fe}_{49.3}\text{Rh}_{47.8}\text{Pd}_{2.9}$ on cooling and heating in the temperature range 218 – 320 K, as well as for the reference sample $\text{Fe}_{50.4}\text{Rh}_{49.6}$ on cooling in the range 320 – 227 K, were analyzed by Rietveld refinement. It has been found that

all samples contain about 7-9% of the fcc γ -phase. In order to fit the low-temperature neutron diffraction patterns below the FM-AFM phase transition, a model of a mixture of the fcc γ -FeRh phase and AFM bcc structure was suggested. For the high-temperature range above the AFM-FM phase transition, a model of a mixture of the fcc γ -phase and FM bcc structure was refined. Finally, the neutron diffraction patterns measured in the AFM-FM phase transition region were modeled by a mixture of the fcc γ -phase, AFM bcc structure, and FM bcc structure. The unit cell parameters of the AFM and FM bcc structures were allowed to be adjusted independently because we were not able to get a good quality of fit for a model where both AFM and FM phases share the same bcc crystal structure model. Thus, we suggested that every sample contains three different crystal structure domains in the narrow temperature range, where both AFM and FM phases coexist: (i) bcc structure of the AFM domain, (ii) bcc structure of the FM domain and (iii) small amount of the fcc γ -phase persisting in the whole temperature range.

The best fits of the neutron diffraction patterns measured for $\text{Fe}_{48.3}\text{Rh}_{46.8}\text{Pd}_{4.9}$ in the FM state at 320 K, mixed magnetic state at the AFM-FM phase transition temperature 296 K, and in the AFM magnetic state at 218 K are shown in Fig. 5 Temperature dependence of the refined AFM (left panel) and FM (right panel) phase fractions (see in the text) plotted for $\text{Fe}_{48.3}\text{Rh}_{46.8}\text{Pd}_{4.9}$, $\text{Fe}_{49.3}\text{Rh}_{47.8}\text{Pd}_{2.9}$ and $\text{Fe}_{50.4}\text{Rh}_{49.6}$. The strong AFM Bragg peak ($\frac{1}{2} \frac{1}{2} \frac{1}{2}$) observed in the low q -range of the D1 detector bank shows a tendency to be suppressed by temperature above the phase transition temperature ~ 296 K. On the contrary, the (100) Bragg peak shows a substantial FM contribution at high temperatures, while no FM contribution is observed at the low temperatures below the phase transition.

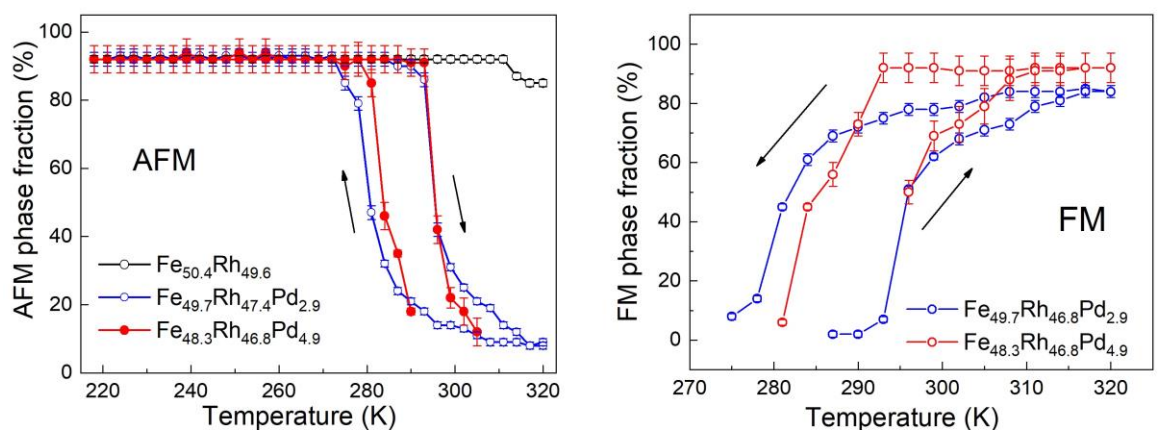


Fig. 5 Temperature dependence of the refined AFM (left panel) and FM (right panel) phase fractions (see in the text) plotted for $\text{Fe}_{48.3}\text{Rh}_{46.8}\text{Pd}_{4.9}$, $\text{Fe}_{49.3}\text{Rh}_{47.8}\text{Pd}_{2.9}$ and $\text{Fe}_{50.4}\text{Rh}_{49.6}$.

The refined values of AFM and FM phase fractions are shown in Fig. 5 Temperature dependence of the refined AFM (left panel) and FM (right panel) phase fractions (see in the text)

plotted for $\text{Fe}_{48.3}\text{Rh}_{46.8}\text{Pd}_{4.9}$, $\text{Fe}_{49.3}\text{Rh}_{47.8}\text{Pd}_{2.9}$ and $\text{Fe}_{50.4}\text{Rh}_{49.6}$. Fig. 5 Temperature dependence of the refined AFM (left panel) and FM (right panel) phase fractions (see in the text) plotted for $\text{Fe}_{48.3}\text{Rh}_{46.8}\text{Pd}_{4.9}$, $\text{Fe}_{49.3}\text{Rh}_{47.8}\text{Pd}_{2.9}$ and $\text{Fe}_{50.4}\text{Rh}_{49.6}$. As one can see, both $\text{Fe}_{48.3}\text{Rh}_{46.8}\text{Pd}_{4.9}$ and $\text{Fe}_{49.3}\text{Rh}_{47.8}\text{Pd}_{2.9}$ samples exhibit substantial thermomagnetic hysteresis on the cooling-heating curves around the AFM-FM phase transition. The phase transition from pure FM phase to the pure AFM phase is extended over a wide temperature range of about ~ 15 K for $\text{Fe}_{48.3}\text{Rh}_{46.8}\text{Pd}_{4.9}$ and about ~ 35 K for $\text{Fe}_{49.3}\text{Rh}_{47.8}\text{Pd}_{2.9}$. The phase transition in pure $\text{Fe}_{50.4}\text{Rh}_{49.6}$ occurs at a higher temperature (~ 323.5 K, well known from elsewhere [34]) and is not shown in the considered temperature range. A slight decrease of the AFM phase fraction develops in the pure $\text{Fe}_{50.4}\text{Rh}_{49.6}$ on approach to the AFM-FM transition above 314 K, as is expected in accordance with the magnetic measurements data [34].

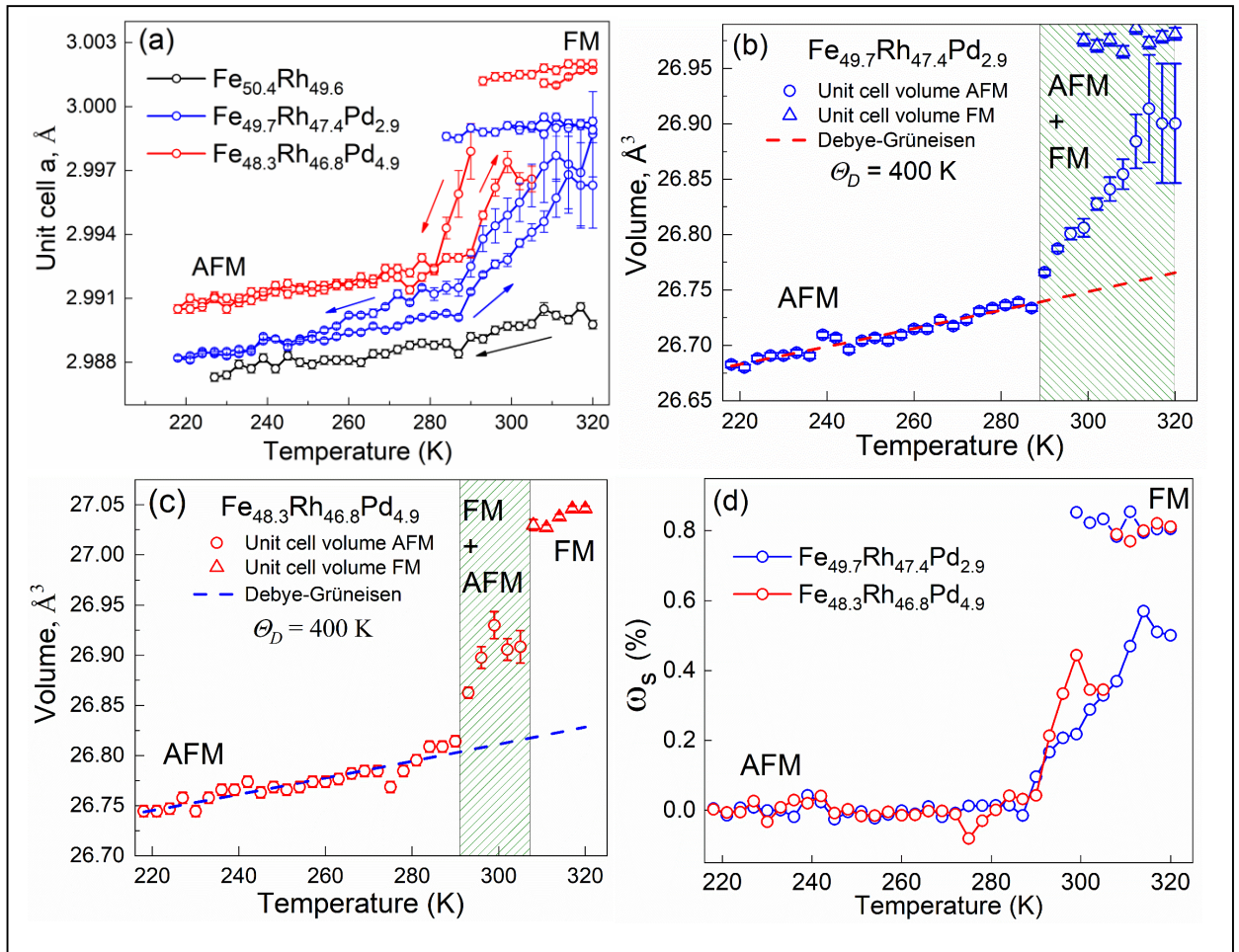


Fig. 6 Temperature dependencies of the (a) refined unit cell parameters on heating and cooling procedures for $\text{Fe}_{48.3}\text{Rh}_{46.8}\text{Pd}_{4.9}$, $\text{Fe}_{49.3}\text{Rh}_{47.8}\text{Pd}_{2.9}$ and $\text{Fe}_{50.4}\text{Rh}_{49.6}$; (b) unit cell volume of $\text{Fe}_{49.3}\text{Rh}_{47.8}\text{Pd}_{2.9}$ fitted by the Debye-Grüneisen law; (c) unit cell volume of $\text{Fe}_{48.3}\text{Rh}_{46.8}\text{Pd}_{4.9}$ fitted by the Debye-Grüneisen law; (d) spontaneous magnetostriction for $\text{Fe}_{48.3}\text{Rh}_{46.8}\text{Pd}_{4.9}$, $\text{Fe}_{49.3}\text{Rh}_{47.8}\text{Pd}_{2.9}$.

Temperature dependencies of the refined unit cell parameters of the AFM phase and FM phase are plotted in Fig. 6(a) for $\text{Fe}_{48.3}\text{Rh}_{46.8}\text{Pd}_{4.9}$, $\text{Fe}_{49.3}\text{Rh}_{47.8}\text{Pd}_{2.9}$ and $\text{Fe}_{50.4}\text{Rh}_{49.6}$. Narrow

hysteresis behavior can be seen on the cooling-heating curves for the $\text{Fe}_{48.3}\text{Rh}_{46.8}\text{Pd}_{4.9}$ sample while it is extended over a wider temperature range in the case of $\text{Fe}_{49.3}\text{Rh}_{47.8}\text{Pd}_{2.9}$. All the plotted curves exhibit a jump-like change of the unit cell parameters in the region of the AFM-FM phase transition for Pd-doped samples. In order to estimate spontaneous volume magnetostriction, the temperature dependencies of the unit cell volume were fitted using the Debye-Grüneisen approximation [46]. The Estimated spontaneous volume magnetostriction is then calculated by $\omega_s = \frac{(V_{\text{exp}} - V_{\text{DG}})}{V_{\text{DG}}} \times 100\%$, where V_{exp} and V_{DG} are the unit cell volumes obtained from the neutron diffraction and Debye-Grüneisen approximation, respectively. The best fit results of the heating curves obtained using fixed Debye temperature $\Theta_D=400\text{K}$ [47] are shown in Figs. 6(b) and (c), while the temperature dependence of the spontaneous volume magnetostriction is shown in Fig. 6(d). It can be seen that ω_s reaches the value $\sim 0.8\%$, which is in a good agreement with the previously reported value of $\omega_s = 8.2 \times 10^{-3}$ in pure iron-rhodium alloys [48]. Bearing in mind the temperature dependencies of the phase fractions (see Fig. 5) and the estimated spontaneous volume magnetostriction, one can suggest that AFM-FM transition in $\text{Fe}_{48.3}\text{Rh}_{46.8}\text{Pd}_{4.9}$ is abrupt while it is more gradual in $\text{Fe}_{49.3}\text{Rh}_{47.8}\text{Pd}_{2.9}$.

We were not able to get a stable solution for magnetic moment values when allowing both Fe and Rh magnetic moments to be refined simultaneously for a FM phase. It was shown previously [31] that the magnetic structure factor can be insensitive to a small changes of Rh magnetic moment. In order to avoid this, the magnetic moment of Rh in the pure FM state was manually fixed to the value $1 \mu_B$ [31,49] while magnetic moment of the Fe sublattice was allowed to be adjusted. The magnetic moment of Fe was estimated to be $\mu(\text{Fe}) = 3.3(1) \mu_B$ for $\text{Fe}_{48.3}\text{Rh}_{46.8}\text{Pd}_{4.9}$ and $\mu(\text{Fe}) = 3.0(1) \mu_B$ for $\text{Fe}_{49.3}\text{Rh}_{47.8}\text{Pd}_{2.9}$ and $\text{Fe}_{50.4}\text{Rh}_{49.6}$ at low temperatures in the AFM state, which is in agreement with the previously published data [50,51]. The magnetic moment of Fe atoms was found to be substantially lower ($\mu(\text{Fe}) = 2.3(2) \mu_B$ for $\text{Fe}_{48.3}\text{Rh}_{46.8}\text{Pd}_{4.9}$ and $\mu(\text{Fe}) = 2.5(2) \mu_B$ for $\text{Fe}_{49.3}\text{Rh}_{47.8}\text{Pd}_{2.9}$) above the AFM-FM transition in the pure FM state (the measured time-averaged moment is expectedly lower than the computed at 0 K value in Table 1).

Hall probe imaging

To confirm the assumptions about **the coexistence of magnetic phases in these alloys**, the magnetic structure during the transition of $\text{Fe}_{48.3}\text{Rh}_{46.8}\text{Pd}_{4.9}$ was analyzed using scanning Hall probe imaging. This method allowed not only confirmation of the presence of magnetic structures, but also tracing of the spatial distribution of magnetization changes during the magnetic phase transition over the sample. The visualization results are presented in Fig. 7.

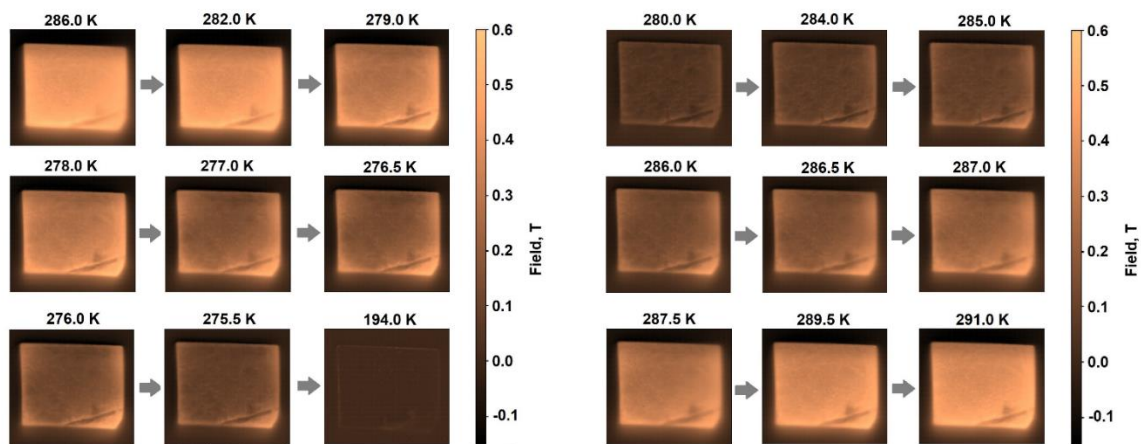


Fig. 7 Series (top to bottom) of scanning Hall probe imaging captures of a $\text{Fe}_{48.3}\text{Rh}_{46.8}\text{Pd}_{4.9}$ sample on cooling (left panel) and heating (right panel) with 1 T magnetic field applied out of the page showing the FM-AFM and AFM-FM transition, respectively. Each image window is 4.1 mm by 3.7 mm with pixel size (and therefore, resolution) of $15 \times 15 \mu\text{m}^2$, and the scale bar indicates the strength of the stray field emitted by the sample in tesla. The whole series can be viewed as a video included in the Supporting Information.

Since the FM phase has finite magnetization and AFM has zero, the existence of each can be inferred from the strength of the field signal measured (strong field indicating the former and zero field from the latter), where the fully FM and fully AFM states are represented by the highest and lowest T images, respectively. The curve in Fig. 8 is integrated from the images, representing the whole sample, and can be accordingly considered as representative of the FM/AFM phase fraction. The shape appears to correspond closely to the neutron scattering data and the sharp, hysteretic transitions observed both locally (i.e. for one pixel in Fig. 9) and for the sample as a whole demonstrate the first-order nature.

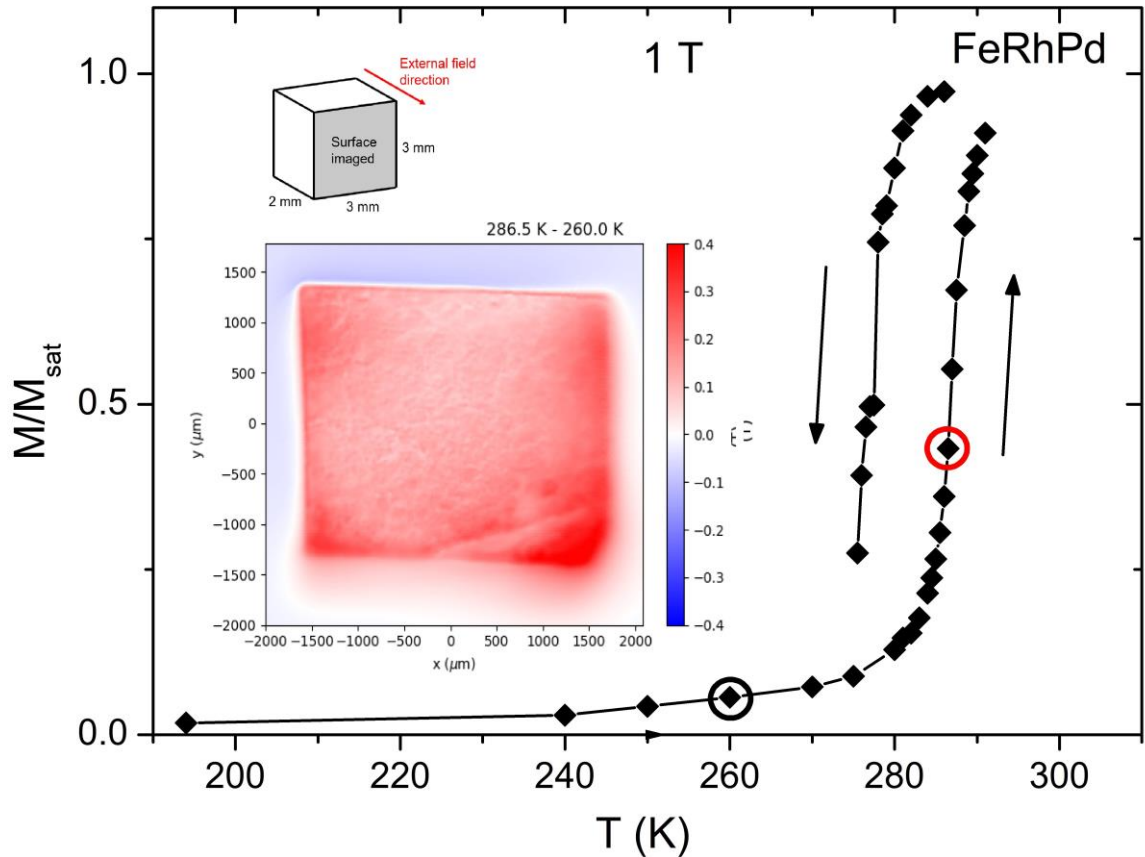


Fig. 8 Moment (normalised to the saturated FM moment) of the thermal transition, extracted from Hall probe imaging data in 1 T. Inset: **upper:** the imaged surface of the cuboid $\text{Fe}_{48,3}\text{Rh}_{46,8}\text{Pd}_{4,9}$ sample with the field direction shown by an arrow; **bottom:** the image at 286.5 K on warming (designated by the red circle), part-way through the transition, subtracting the image at 260 K before the transition (black circle), showing the change in the spatial distribution of moment.

Transformation occurs predominantly on the microscale (smaller than the $15\ \mu\text{m}$ pixel size), not the macro-scale, since no distinct boundary is observed in the images. This can be seen in Fig. 9, but is also shown clearly by the inset in Fig. 8, which presents the change in field signal across the sample surface between a temperature prior to the onset of the FM transition and a temperature midway through: here a positive change in detected field indicates the existence of regions which have transformed into the FM state, and these can be seen to have occurred everywhere across the sample, despite the transition to FM being less than halfway progressed. Instead, the incomplete nature of the transition manifests as varying intensity on the local/pixel scale. Since we can assume that FM regions will be magnetically aligned with the field (because the applied field is considerable), we conclude that such intensity variation is caused by varying mixes of FM/AFM regions generally on a scale smaller than we are able to detect. Note that the line at the bottom right of the sample is a topographical recess feature in the surface, which is not related to a magnetic structure. We should however discuss the nature of a surface magnetic measurement

technique and to what degree it can be confidently said to represent the entire sample: here we have intentionally measured the largest surface, so that internal volume not probed is minimized, and applied a strong field perpendicular to the surface, so that any FM regions will strongly align with it (and with the direction of Hall probe sensitivity). It is possible that regions deeper in the sample are not adjacently detected and could contribute to a weaker signal detected at the surface due to spreading of the resulting field lines with distance; however, the existence of FM regions throughout the sample is clear, despite the transformation being incomplete for many of the images, where any macroscale FM-only regions (which did occur, even if deeper in the sample) would be expected to give distinct concentrated field profiles at the surface for this ratio of sample thickness to surface length (2:3), which is not universally observed across the surface; the dominance of demagnetizing fields (discussed next) would mean a similar profile should be observed at each level of depth beneath the surface for this external field direction; and lastly no evidence of the surface region (to which the technique is very sensitive) having a sharp phase boundary is observed – this can be contrasted with the same imaging technique on similar sample geometries of the $\text{La}(\text{Fe},\text{Si})_{13}$ family [52,53], where more strongly macroscale-dominated phase mixing is evident. Thus, we can be confident that the surface measurement is reliable for the conclusions we make.

There remains the question of whether the phase coexistence occurs within grains or inter-grain where each grain undergoes transformation homogeneously. Although the pixel size is close to the size of the grains we conclude that we are currently not able to distinguish between these possibilities because both the Hall sensor distance of 10 μm from the surface and sensitivity to several layers of grains below the surface leads to “smearing” of the magnetic signal from each, and thus an inability to resolve single grains.

During the first stage of the FM transition, the concentration of transformation is stronger at the sample edges (and somewhat around the surface recess feature described in the previous paragraph) and spreads in from there with increased T ; equivalently, the early stages of the AFM transition on cooling occurs predominantly in the central regions of the surface. This is indicative of demagnetising fields, rather than microstructure, dominating the transition: the high-magnetization FM and low/zero magnetization AFM regions during the period of phase coexistence are more concentrated in the regions of high and low internal field, respectively, in the presence of external field, which is determined by the effect of demagnetizing fields specific to the sample shape and direction of external field. This dominance is a result of no/very little magnetocrystalline anisotropy of the cubic material – a similar dominance is seen at the magnetovolume transition in cubic $\text{La}(\text{Fe},\text{Si})_{13}$ family of materials [52,53].

Thus, according to direct visualization of phase dynamics, the mixed phase is microscopic, at least compared to the 15 micron resolution of this Hall probe. One can see sharp hysteretic phase transitions both locally and the sample as a whole, an additional support for first-order behavior. The transition comes in from the edges of the sample, so demagnetization effects and sample shape dominate. There must therefore be little or no magnetocrystalline anisotropy, which is consistent with it being a cubic crystalline phase.

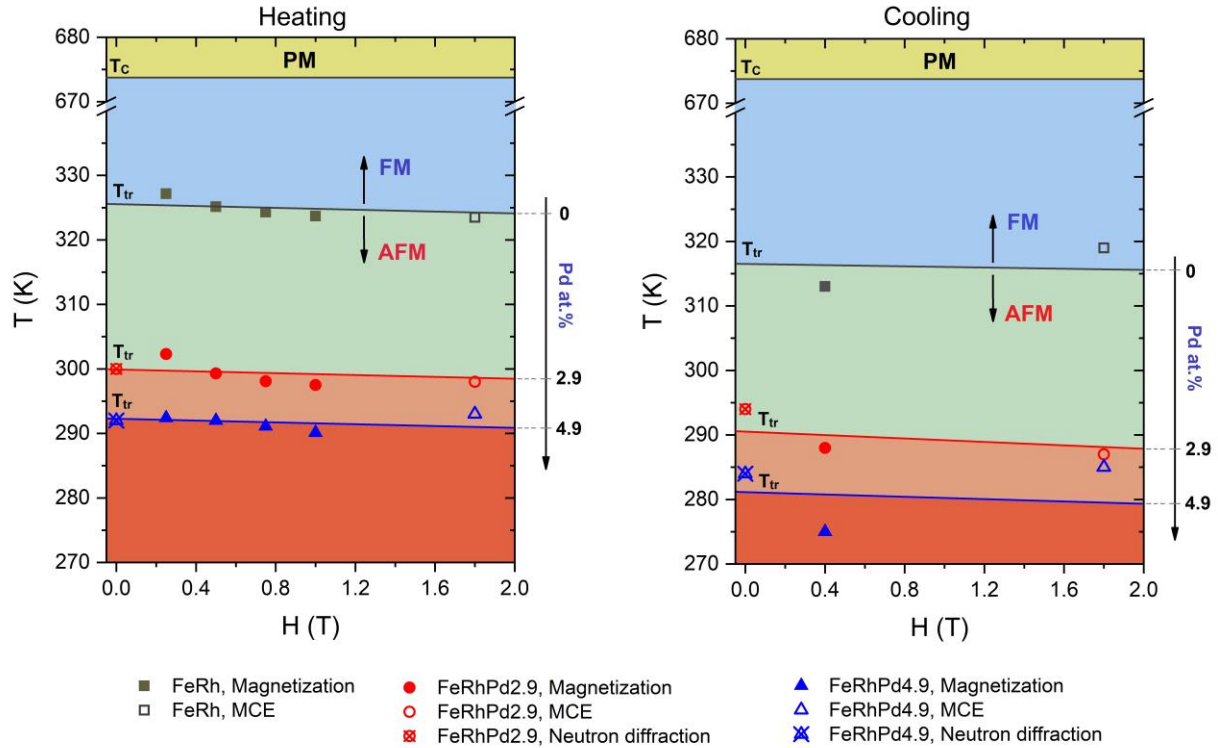


Fig. 9. Magnetic phase diagram of $\text{Fe}_{50.4}\text{Rh}_{49.6}$, $\text{Fe}_{49.7}\text{Rh}_{47.4}\text{Pd}_{2.9}$ and $\text{Fe}_{48.3}\text{Rh}_{46.8}\text{Pd}_{4.9}$ on heating (left panel) and cooling (right panel) Magnetization, magnetocaloric effect data have been taken from [34,35], neutron diffraction data obtained in the present work.

Magnetization and magnetocaloric effect were measured in our previous works [34,35] using the same samples. Magnetization measurements were performed using a vibrating sample magnetometer (VSM, Toei Co Ltd. model-5) with a sweep rate of 1K/min. The magnetic field dependence of the MCE was measured at different temperatures in the region of the first order AFM–FM phase transition, and the temperature dependence of the MCE in the largest magnetic field of 1.8 T was obtained by direct measurement using the automated MCE measuring setup (MagEq MMS 801, AMT&C LLC). Magnetic phase diagrams for a series of palladium alloys and their dependence on Pd concentration on both heating and cooling have not been published before. On heating (left panel) all the studied alloys are ferromagnets in the temperature range below the Curie temperature ($T_C = 675$ K for $\text{Fe}_{50.4}\text{Rh}_{49.6}$) of the FM-PM transition and above the FOMT temperature of the AFM-FM transition (which is different for each of studied alloys), where the phase transformation into antiferromagnetic state occurs. It is possible to note a monotonic but

nonlinear shift of the AFM-FM phase boundary towards lower temperatures with increase of the palladium concentration (as well as with higher Rh fraction in Fe-Rh); the rate of transition temperature decrease is not proportional to the change of the relative palladium content in alloys. This circumstance, apparently, is also connected with the solubility limit of palladium in Fe-Rh alloy, exceeding of which results in formation of FePd precipitates with another type of crystal structure. Comparing the transition temperature for cooling and heating, one can see a large temperature hysteresis (~7-9 K) for each alloy. This hysteresis provides additional evidence for the first-order nature of the transition.

CONCLUSIONS

In this work, the determination of the main parameters of magnetic structures of the family of iron-rhodium alloys $\text{Fe}_{50,4}\text{Rh}_{49,6}$, $\text{Fe}_{49,7}\text{Rh}_{47,4}\text{Pd}_{2,9}$ and $\text{Fe}_{48,3}\text{Rh}_{46,8}\text{Pd}_{4,9}$ was, for the first time, performed. Direct measurements made it possible to show quantitatively the change of AFM and FM phase fractions in the area of coexistence of AFM and FM phases, as well as the dynamics of magnetic transition. The area of phase co-existence was found in the temperature range of 290 K - 320 K on heating and 275 K - 310 K on cooling. Hysteresis behavior of the main parameters (FM and AFM phases' weight fractions, lattice constant of the unit cell) was observed to be proportional to the Pd concentration in doped alloys. Phase diagrams of a series of palladium-substituted rhodium alloys both on heating and cooling were constructed to analyze the dependence of the phase transformation on the Pd concentration and show the hysteresis of the phase transition temperature. Complementary scanning Hall probe imaging fully supports the existence of mixing of phases and visually demonstrates that mixing occurs on the microscale, while the spatial distribution of the transition is dominated by demagnetization effects, showing parallels with transition properties observed in another cubic material, $\text{La}(\text{Fe},\text{Si})_{13}$ [52,53] in contrast to the evolution of the transition in polycrystalline materials with strong magnetocrystalline anisotropy such as Gd_5Ge_4 [54,55]. **Magnetic imaging gives additional information, specifically spatial distribution of the phase transition and transition property lengthscales can be obtained from it.** The practical importance of considering the doped alloys consists in the shift of the phase transition to lower temperature without a significant reduction of their magnetothermal properties, compared with the initial equiatomic iron-rhodium alloy with transition around 353 K, above room temperature [33].

ACKNOWLEDGEMENTS

EL acknowledges funding from the UK EPSRC. LC acknowledges funding from the EPSRC and InnovateUK: Project number: 105541. A portion of this research used resources at the Spallation Neutron Source, a DOE Office of Science User Facility operated by the Oak Ridge

National Laboratory. This work was partly supported by the state assignment of the Ministry of Education and Science of Russia (themes “Flux” No. AAAA-A18-118020190112-8 and “Alloys” № AAAA-A19-119070890020-3).

REFERENCES

1. Dagotto, E. Open questions in CMR manganites, relevance of clustered states and analogies with other compounds including the cuprates. *New J. Phys.* **2005**, *7*, 67–67, doi:10.1088/1367-2630/7/1/067.
2. Roy, S.B.; Perkins, G.K.; Chattopadhyay, M.K.; Nigam, A.K.; Sokhey, K.J.S.; Chaddah, P.; Caplin, A.D.; Cohen, L.F. First Order Magnetic Transition in Doped CeFe_2 Alloys: Phase Coexistence and Metastability. *Phys. Rev. Lett.* **2004**, *92*, 147203, doi:10.1103/PhysRevLett.92.147203.
3. Pecharsky, V.K.; Gschneidner, Jr., K.A. Giant Magnetocaloric Effect in $\text{Gd}_5(\text{Si}_2\text{Ge}_2)$. *Phys. Rev. Lett.* **1997**, *78*, 4494–4497, doi:10.1103/PhysRevLett.78.4494.
4. Ahn, K.H.; Lookman, T.; Bishop, A.R. Strain-induced metal-insulator phase coexistence in perovskite manganites. *Nature* **2004**, *428*, 401–404, doi:10.1038/nature02364.
5. Uehara, M.; Mori, S.; Chen, C.H.; Cheong, S.-W. Percolative phase separation underlies colossal magnetoresistance in mixed-valent manganites. *Nature* **1999**, *399*, 560–563, doi:10.1038/21142.
6. Fallot, M. *Ann. Phys. (Paris)* **1938**, *10*, 291.
7. Mariager, S.O.; Pressacco, F.; Ingold, G.; Caviezel, A.; Möhr-Vorobeva, E.; Beaud, P.; Johnson, S.L.; Milne, C.J.; Mancini, E.; Moyerman, S.; et al. Structural and Magnetic Dynamics of a Laser Induced Phase Transition in FeRh. *Phys. Rev. Lett.* **2012**, *108*, 087201, doi:10.1103/PhysRevLett.108.087201.
8. Gray, A.X.; Cooke, D.W.; Krüger, P.; Bordel, C.; Kaiser, A.M.; Moyerman, S.; Fullerton, E.E.; Ueda, S.; Yamashita, Y.; Gloskovskii, A.; et al. Electronic Structure Changes across the Metamagnetic Transition in FeRh via Hard X-Ray Photoemission. *Phys. Rev. Lett.* **2012**, *108*, 257208, doi:10.1103/PhysRevLett.108.257208.
9. Cooke, D.W.; Hellman, F.; Baldasseroni, C.; Bordel, C.; Moyerman, S.; Fullerton, E.E. Thermodynamic Measurements of Fe-Rh Alloys. *Phys. Rev. Lett.* **2012**, *109*, 255901, doi:10.1103/PhysRevLett.109.255901.
10. Derlet, P.M. Landau-Heisenberg Hamiltonian model for FeRh. *Phys. Rev. B* **2012**, *85*, 174431, doi:10.1103/PhysRevB.85.174431.
11. Vries, M.A. de; Loving, M.; Mihai, A.P.; Lewis, L.H.; Heiman, D.; Marrows, C.H. Hall-effect characterization of the metamagnetic transition in FeRh. *New J. Phys.* **2013**, *15*, 013008, doi:10.1088/1367-2630/15/1/013008.
12. Staunton, J.B.; Banerjee, R.; Dias, M. dos S.; Deak, A.; Szunyogh, L. Fluctuating local moments, itinerant electrons, and the magnetocaloric effect: Compositional hypersensitivity of FeRh. *Phys. Rev. B* **2014**, *89*, 054427, doi:10.1103/PhysRevB.89.054427.
13. Neves Bez, H.; Pathak, A.K.; Biswas, A.; Zarkevich, N.; Balema, V.; Mudryk, Y.; Johnson, D.D.; Pecharsky, V.K. Giant enhancement of the magnetocaloric response in Ni–Co–Mn–Ti by rapid solidification. *Acta Materialia* **2019**, *173*, 225–230, doi:10.1016/j.actamat.2019.05.004.
14. Zarkevich, N.A.; Zverev, V.I. Viable Materials with a Giant Magnetocaloric Effect. *Crystals* **2020**, *10*, 815, doi:10.3390/cryst10090815.
15. Tishin, A.M.; Rochev, J.A.; Gorelov, A.V. Magnetic carrier and medical preparation for controllable delivery and release of active substances, a method of production and method of treatment using thereof 2008.
16. Tishin, A.M.; Rochev, J.A.; Gorelov, A.V. Magnetic carrier and medical preparation for controllable delivery and release of active substances, a method of production and method of treatment using thereof 2009.

17. Thiele, J.-U.; Maat, S.; Fullerton, E.E. FeRh/FePt exchange spring films for thermally assisted magnetic recording media. *Applied Physics Letters* **2003**, *82*, 2859–2861, doi:10.1063/1.1571232.
18. Ricodeau, J.A.; Melville, D. Model of the antiferromagnetic-ferromagnetic transition in FeRh alloys. *J. Phys. F: Met. Phys.* **1972**, *2*, 337, doi:10.1088/0305-4608/2/2/024.
19. Valiev, E.; Gimaev, R.; Zverev, V.; Kamilov, K.; Pyatakov, A.; Kovalev, B.; Tishin, A. Application of the exchange-striction model for the calculation of the FeRh alloys magnetic properties. *Intermetallics* **2019**, *108*, 81–86, doi:10.1016/j.intermet.2019.02.015.
20. Belov, M.P.; Syzdykova, A.B.; Abrikosov, I.A. Temperature-dependent lattice dynamics of antiferromagnetic and ferromagnetic phases of FeRh. *Phys. Rev. B* **2020**, *101*, 134303, doi:10.1103/PhysRevB.101.134303.
21. Manekar, M.; Mukherjee, C.; Roy, S.B. Imaging of time evolution of the first-order magneto-structural transition in Fe-Rh alloy using magnetic force microscopy. *EPL* **2007**, *80*, 17004, doi:10.1209/0295-5075/80/17004.
22. Maat, S.; Thiele, J.-U.; Fullerton, E.E. Temperature and field hysteresis of the antiferromagnetic-to-ferromagnetic phase transition in epitaxial FeRh films. *Phys. Rev. B* **2005**, *72*, 214432, doi:10.1103/PhysRevB.72.214432.
23. Yokoyama, Y.; Usukura, M.; Yuasa, S.; Suzuki, Y.; Miyajima, H.; Katayama, T. MFM observation of magnetic phase transitions in ordered FeRh systems. *Journal of Magnetism and Magnetic Materials* **1998**, *177–181*, 181–182, doi:10.1016/S0304-8853(97)00953-0.
24. Kouvel, J.S. Unusual Nature of the Abrupt Magnetic Transition in FeRh and Its Pseudobinary Variants. *Journal of Applied Physics* **1966**, *37*, 1257–1258, doi:10.1063/1.1708424.
25. Baranov, N.V.; Barabanova, E.A. Electrical resistivity and magnetic phase transitions in modified FeRh compounds. *Journal of Alloys and Compounds* **1995**, *219*, 139–148, doi:10.1016/0925-8388(94)01375-6.
26. Schinkel, C.J.; Hartog, R.; Hochstenbach, F.H.A.M. On the magnetic and electrical properties of nearly equiatomic ordered FeRh alloys. *J. Phys. F: Met. Phys.* **1974**, *4*, 1412, doi:10.1088/0305-4608/4/9/013.
27. Kushwaha, P.; Bag, P.; Rawat, R.; Chaddah, P. First-order antiferro–ferromagnetic transition in Fe₄₉(Rh_{0.93}Pd_{0.07})₅₁ under simultaneous application of magnetic field and external pressure. *J. Phys.: Condens. Matter* **2012**, *24*, 096005, doi:10.1088/0953-8984/24/9/096005.
28. Kushwaha, P.; Lakhani, A.; Rawat, R.; Chaddah, P. Low-temperature study of field-induced antiferromagnetic-ferromagnetic transition in Pd-doped Fe-Rh. *Phys. Rev. B* **2009**, *80*, 174413, doi:10.1103/PhysRevB.80.174413.
29. Muldrew, L.; deBergevin, F. Antiferromagnetic-Ferromagnetic Transformation in FeRh. *The Journal of Chemical Physics* **1961**, *35*, 1904–1905, doi:10.1063/1.1732175.
30. Shirane, G.; Chen, C.W.; Flinn, P.A.; Nathans, R. Hyperfine Fields and Magnetic Moments in the Fe–Rh System. *Journal of Applied Physics* **1963**, *34*, 1044–1045, doi:10.1063/1.1729362.
31. Shirane, G.; Nathans, R.; Chen, C.W. Magnetic Moments and Unpaired Spin Densities in the Fe-Rh Alloys. *Phys. Rev.* **1964**, *134*, A1547–A1553, doi:10.1103/PhysRev.134.A1547.
32. Kren, E.; Pal, L.; Szabo, P. Neutron diffraction investigation of the antiferromagnetic-ferromagnetic transformation in the FeRh alloy. *Physics Letters* **1964**, *9*, 297–298, doi:10.1016/0031-9163(64)90369-5.
33. Zarkevich, N.A.; Johnson, D.D. FeRh ground state and martensitic transformation. *Phys. Rev. B* **2018**, *97*, 014202, doi:10.1103/PhysRevB.97.014202.
34. Zverev, V.I.; Saletsky, A.M.; Gimaev, R.R.; Tishin, A.M.; Miyanaga, T.; Staunton, J.B. Influence of structural defects on the magnetocaloric effect in the vicinity of the first order magnetic transition in Fe_{50.4}Rh_{49.6}. *Applied Physics Letters* **2016**, *108*, 192405, doi:10.1063/1.4949355.

35. Gimaev, R.; Zverev, V.; Spichkin, Y.; Tishin, A.; Miyanaga, T. Peculiarities of the magnetocaloric effect in FeRh-based alloys in the vicinity of the first order magnetic phase transition. *EPJ Web Conf.* **2018**, *185*, 05008, doi:10.1051/epjconf/201818505008.
36. Zarkevich, N. Structural database for reducing cost in materials design and complexity of multiscale computations. *Complexity* **2006**, *11*, 36–42, doi:10.1002/cplx.20117.
37. Johnson, D.D.; Nicholson, D.M.; Pinski, F.J.; Gyorffy, B.L.; Stocks, G.M. Density-Functional Theory for Random Alloys: Total Energy within the Coherent-Potential Approximation. *Phys. Rev. Lett.* **1986**, *56*, 2088–2091, doi:10.1103/PhysRevLett.56.2088.
38. Johnson, D.D.; Smirnov, A.V.; Khan, S.N. *MECCA: Multiple-Scattering Electronic-Structure Calculations for Complex Alloys. KKR-CPA Program, Ver. 2.0*, Iowa State University and Ames Laboratory, Ames; 2015;
39. Perdew, J.P.; Ruzsinszky, A.; Csonka, G.I.; Vydrov, O.A.; Scuseria, G.E.; Constantin, L.A.; Zhou, X.; Burke, K. Restoring the Density-Gradient Expansion for Exchange in Solids and Surfaces. *Phys. Rev. Lett.* **2008**, *100*, 136406, doi:10.1103/PhysRevLett.100.136406.
40. Monkhorst, H.J.; Pack, J.D. Special points for Brillouin-zone integrations. *Phys. Rev. B* **1976**, *13*, 5188–5192, doi:10.1103/PhysRevB.13.5188.
41. Zarkevich, N.A.; Johnson, D.D. Reliable thermodynamic estimators for screening caloric materials. *Journal of Alloys and Compounds* **2019**, *802*, 712–722, doi:10.1016/j.jallcom.2019.06.150.
42. Alam, A.; Khan, S.N.; Wilson, B.G.; Johnson, D.D. Efficient isoparametric integration over arbitrary space-filling Voronoi polyhedra for electronic structure calculations. *Phys. Rev. B* **2011**, *84*, 045105, doi:10.1103/PhysRevB.84.045105.
43. Neuefeind, J.; Feygenson, M.; Carruth, J.; Hoffmann, R.; Chipley, K.K. The Nanoscale Ordered Materials Diffractometer NOMAD at the Spallation Neutron Source SNS. *Nuclear Instruments and Methods in Physics Research Section B: Beam Interactions with Materials and Atoms* **2012**, *287*, 68–75, doi:10.1016/j.nimb.2012.05.037.
44. Rodríguez-Carvajal, J. Recent advances in magnetic structure determination by neutron powder diffraction. *Physica B: Condensed Matter* **1993**, *192*, 55–69, doi:10.1016/0921-4526(93)90108-I.
45. Balagurov, A.M.; Pomjakushin, V.Yu.; Sheptyakov, D.V.; Aksenov, V.L.; Fischer, P.; Keller, L.; Gorbenko, O.Yu.; Kaul, A.R.; Babushkina, N.A. Long-scale phase separation versus homogeneous magnetic state in $(\text{La}_{1-y}\text{Pr}_y)\text{0.7Ca0.3MnO}_3$: A neutron diffraction study. *Phys. Rev. B* **2001**, *64*, 024420, doi:10.1103/PhysRevB.64.024420.
46. Sayetat, F.; Fertey, P.; Kessler, M. An Easy Method for the Determination of Debye Temperature from Thermal Expansion Analyses. *J Appl Cryst* **1998**, *31*, 121–127, doi:10.1107/S0021889897006936.
47. Kreiner, K.; Michor, H.; Hilscher, G.; Baranov, N.V.; Zemlyanski, S.V. Evolution of the electronic specific heat and magnetic order in $(\text{Fe}_{1-x}\text{Ni}_x)\text{Rh}$. *Journal of Magnetism and Magnetic Materials* **1998**, *177–181*, 581–582, doi:10.1016/S0304-8853(97)00282-5.
48. Ibarra, M.R.; Algarabel, P.A. Giant volume magnetostriction in the FeRh alloy. *Phys. Rev. B* **1994**, *50*, 4196–4199, doi:10.1103/PhysRevB.50.4196.
49. Moruzzi, V.L.; Marcus, P.M. Antiferromagnetic-ferromagnetic transition in FeRh. *Phys. Rev. B* **1992**, *46*, 2864–2873, doi:10.1103/PhysRevB.46.2864.
50. Nishimura, K.; Nakazawa, Y.; Li, L.; Mori, K. Magnetocaloric Effect of $\text{Fe}(\text{Rh}_{1-x}\text{Pdx})$ Alloys. *Materials Transactions* **2008**, *49*, 1753–1756, doi:10.2320/matertrans.MRA2008080.
51. Lu, W.; Nam, N.T.; Suzuki, T. Effect of Pt Doping on the Structure, Magnetic, and Magneto-Optical Properties of Ordered FeRh-Pt Thin Films. *IEEE Transactions on Magnetics* **2009**, *45*, 2716–2719, doi:10.1109/TMAG.2009.2018650.
52. Lovell, E.; Pereira, A.M.; Caplin, A.D.; Lyubina, J.; Cohen, L.F. Dynamics of the First-Order Metamagnetic Transition in Magnetocaloric $\text{La}(\text{Fe,Si})_{13}$: Reducing Hysteresis. *Advanced Energy Materials* **2015**, *5*, 1401639, doi:10.1002/aenm.201401639.

53. Lovell, E.; Morrison, K.; Pereira, A.M.; Caplin, D.; Gutfleisch, O.; Cohen, L.F. Scanning Hall Probe Imaging of LaFe_{13-x}Si_x Available online: /AST.93.219 (accessed on Apr 25, 2020).
54. Moore, J.D.; Perkins, G.K.; Bugoslavsky, Y.; Cohen, L.F.; Chattopadhyay, M.K.; Roy, S.B.; Chaddah, P.; Gschneidner, K.A.; Pecharsky, V.K. Correlating the local magnetic properties of the magnetic phase transition in Gd₅Ge₄ using scanning Hall probe imaging. *Phys. Rev. B* **2006**, *73*, 144426, doi:10.1103/PhysRevB.73.144426.
55. Moore, J.D.; Perkins, G.K.; Morrison, K.; Ghivelder, L.; Chattopadhyay, M.K.; Roy, S.B.; Chaddah, P.; Jr, K.A.G.; Pecharsky, V.K.; Cohen, L.F. Local probing of arrested kinetics in Gd₅Ge₄. *J. Phys.: Condens. Matter* **2008**, *20*, 465212, doi:10.1088/0953-8984/20/46/465212.

Conflict of interests

The authors declare that they have no known competing financial interests or personal relationships that could have appeared to influence the work reported in this paper.

Vladimir I. Zverev	Conceptualization Methodology Validation Investigation Writing - Original Draft Writing - Review & Editing Supervision
Radel R. Gimaev	Investigation Writing - Original Draft Visualization
Takafumi Miyanaga	Investigation Resources
Artem A. Vaulin	Software Formal analysis Investigation Visualization
Andrey F. Gubkin	Conceptualization Methodology Validation Formal analysis Investigation Resources Writing - Original Draft Writing - Review & Editing
Boris B. Kovalev	Validation Writing - Review & Editing Visualization
Antonio M. dos Santos	Software Formal analysis Writing - Original Draft
Edmund Lovell	Investigation Writing - Original Draft Visualization
Lesley F. Cohen	Conceptualization Resources Writing - Review & Editing Supervision

Nikolai A. Zarkevich	Methodology Software Validation Formal analysis Writing - Original Draft Writing - Review & Editing